Flow Enthalpy of Non-equilibrium Plasma in 1 MW Class Arc-heated Wind Tunnel

Yusuke Takahashi[1], Naoya Enoki[2], Taiki Koike[3],
Hokkaido University, Kita 13 Nishi 8, Kita-ku, Sapporo, Hokkaido 060-8628, Japan
and
Mayuko Tanaka[4],
Waseda University, 1-104 Totsukamachi, Shinjuku-ku, Tokyo, 169-8050, Japan
and
Kazuhiko Yamada[5], and Takayuki Shimoda[6]
Japan Aerospace Exploration Agency, 3-1-1 Yoshinodai Chuo-ku, Sagamihara, Kanagawa 252-5210, Japan

Abstract

The flow enthalpy of an arc-heated wind tunnel is an important parameter for reproducing planetary entry and performing heating tests. However, its distribution is insufficiently clarified owing to complicated phenomena, such as arc discharge and supersonic expansion. In this study, we assess the enthalpy of an arc-heated flow in a large-scale facility based on measurements and computational results. The flow enthalpy of high-temperature gases, which comprised thermal, chemical, kinetic, and pressure components, was reconstructed based on the measured rotational temperature, heat flux, and impact pressure, in addition to the computational science approach. The rotational temperature of nitric oxide molecules was obtained using emission spectroscopic measurements of band spectra in the near-ultraviolet range. A numerical model was developed and validated based on measured data. The results indicated that the model efficiently reproduced the arc discharge behavior in the heating section and the thermochemical non-equilibrium in the expansion section. It was discovered that the dominant components of the arc-heated flow in the test section were the chemical and kinetic components. The flow enthalpy exhibited a non-uniform distribution in the radial direction. We conclude that the flow enthalpy of the core is approximately 28 MJ/kg at the nozzle exit.

Nomenclature

C	=	mass fraction
D	=	effective diffusion coefficient, m^2/s
e	=	energy per unit mass, J/kg
h	=	enthalpy, J/kg
H_{ave}	=	mass-averaged enthalpy, J/kg
Δh^0	=	enthalpy of formation, J/kg
k	=	Boltzmann constant, J/K
M	=	molar mass, kg/mol
N_{A}	=	Avogadro constant, 1/mol

[1]Assistant Professor, Faculty of Engineering; ytakahashi@eng.hokudai.ac.jp.
[2]Graduate Student, Graduate School of Engineering.
[3]Graduate Student, Graduate School of Engineering.
[4]Graduate Student, Graduate School of Science and Engineering.
[5]Associate Professor, Institute of Space and Astronautical Science.
[6]Researcher, Institute of Space and Astronautical Science.

ns = number of species
p = pressure, $\mathrm{N/m^2}$
q = heat flux, $\mathrm{W/m^2}$
r = radial coordinate, m
s = species
T = temperature, K
u = velocity, m/s
V = voltage, V
X = mole fraction
γ = recombination coefficient
λ = thermal conductivity, $\mathrm{W/(K{\cdot}m)}$
μ = viscosity, $\mathrm{N{\cdot}s/m^2}$
ρ = density, $\mathrm{kg/m^3}$

Subscripts
c = chamber
ele = electron
rot = rotation
s = species
t = turbulent
trs = translation
vib = vibration
w = wall

Superscripts
con = convection
rad = radiation

1 Introduction

Several sample return missions from outer planets and their moons in the solar system, e.g., the Martian moon exploration [1], Jupiter Trojan asteroid exploration with a solar power sail [2], and life investigation in the Enceladus sample return mission [3], have been proposed. Some of these missions, such as the Hayabusa sample return mission [4, 5] or the Stardust mission [6, 7], include atmospheric reentry phases. Hence, the design and development of sample return capsules, including a thermal protection system, are important for the safety and efficiency of the missions.

The 1 MW arc-heated wind tunnel in the Institute of Space and Aeronautical Science (ISAS) of the Japan Aerospace Exploration Agency is a promising key facility for enabling these missions. However, the distribution of arc-heated flow properties at a particular flow condition remains unclear despite several studies that have investigated arc-heated flows using measurement approaches. The arc-heated wind tunnels are typically composed of a constrictor section and nozzle section, which serve as the heating section and expansion section, respectively. Because supersonic expansion occurs in the nozzle section, strong thermochemical non-equilibrium is observed in many arc-heating facilities. The thermochemical non-equilibrium hinders the accurate measurement of flow field properties and correct opera-

tion of thermal testing using arc-heating facilities. In addition, high-temperature gases (i.e., gases in the arc column) heated by arc discharge near the core and cold gas surrounding the arc column are formed in the constrictor, causing non-uniform distributions of flow properties. A non-uniform distribution occurs in the radial direction at the nozzle exit. However, it is mitigated by a strong mixture of turbulence and radiation. To acquire good quality measurement data, it is essential to identify the arc-heated flow property distribution at the nozzle exit.

Thus far, the Pitot pressure and heat flux of arc-heated flows have been obtained as intrusive diagnostic techniques. The spectroscopic analysis of the molecular band, [8], laser-induced fluorescence (LIF) [9, 10], and cavity-enhanced absorption spectroscopy [11], which are non-intrusive techniques, have been used to identify arc-heated flow properties. The emission spectra of the arc column in a constrictor revealed the distributions of translational temperature, flow velocity, and electron number density in the heating section [12, 13]. Zander et al. [14] directly measured the translational temperature and velocity of a plasma flow using the Fabry–Perot spectroscopic technique. Gülhan et al. [15] revealed the characteristics of high-enthalpy flows in the arc-heated wind tunnel, L3K in the German Aerospace Center (DLR; Deutsches Zentrum für Luft- und Raumfahrt) using various measurement tools, i.e., coherent anti-Stokes Raman scattering, LIF emission spectroscopy, and microwave interferometer methods. Throughout the measurements, the rotational and vibrational temperatures, flow velocity, and electron number density were clarified. Steffens et al. [16] measured the electron number density and electronic excitation temperature of L2K plasma flows in DLR using a Langmuir probe, microwave interferometry, and microwave plasma transmission spectroscopy methods.

Additionally, the mass-averaged enthalpy and local mass-specific enthalpy of arc heaters have been investigated using probe techniques and spectroscopy measurements. The heating rate method (HRM) for a blunt body model was proposed by Marvin and Pope [17], which is one of the standard methods for calculating the stagnation enthalpy [18]. Park et al. [19] investigated the flow enthalpies for large-scale arc heating facilities using a heat balance, a sonic throat, the heating rate, spectroscopy methods, and numerical analysis. Their results indicated that the centerline enthalpy differed significantly from the mass-averaged enthalpy. Löhle et al. [20] suggested a new enthalpy probe for plasma flows to measure local mass-specific enthalpy using mass injection. Hermann et al. [21] investigated the local enthalpy of a plasma wind tunnel at the University of Stuttgart based on VUV–NIR spectroscopic measurements. The enthalpy corresponded to the high-altitude flight condition of the Hayabusa sample return capsule.

Similar to experimental approaches, computational science approaches [22–25] including computational fluid dynamics (CFD) have been used to investigate arc-heated flow properties. Prabhu et al. [26, 27] clarified the flow property profiles of arc jets generated by the 20 MW aerodynamic heating facility (AHF) and the 60 MW interaction heating facility at the National Aeronautics and Space Administration [28] using the CFD approach. Takahashi et al. [29, 30] numerically clarified that the arc-heated flows in the Kyushu University 20 kW wind tunnel exhibited significant thermochemical non-equilibrium owing to the strong supersonic expansion in the nozzle. Because the expansion flow in the nozzle was excited both rotationally and vibrationally, a multi-temperature model introduced in the study, which separated the rotational and vibrational temperatures from the translational temperature, was effectively used for expressing the thermal non-equilibrium. In large arc-heating facilities such as the 20 MW AHF, thermochemical non-equilibrium is reduced, whereas both turbulence and radiation become key factors for the heat transfer from the arc column to

the surrounding cold gas [31]. Thus, sophisticated radiation and turbulence models must be introduced. For the heating process, because the arc discharge affects the plasma formation, the accurate calculation of transport properties, such as the electric conductivity, becomes significant. Katsurayama et al. [32] and Yu et al. [33] indicated that a higher-accuracy transport property model is effective for discharge formation prediction.

Strong demands exist for determining the flow enthalpy, which is an important parameter for simulating the atmospheric reentry environment on the ground. Because it is difficult to evaluate local enthalpy, i.e., the distribution, from the mass-averaged enthalpy, it is desirable to directly determine the local enthalpy. The gas temperature, heat flux, and impact pressure provide useful information for evaluating flow enthalpy. Moreover, a computational science approach has become a powerful tool for investigating such a complex flow field owing to recent developments in high-performance computers and the advancement of algorithms. This approach can reveal flow property distributions in detail, including the flow enthalpy of arc-heated flows. However, the analysis model should be carefully validated. The objective of the present study is to clarify the flow enthalpy in the ISAS 1 MW arc heater using intrusive and non-intrusive measurement techniques as well as compare it with a numerical approach. In addition, we propose a reconstruction method for flow enthalpy determination based on the measured and computed results.

2 ISAS 1 MW Arc Heater

It is worth identifying the rotational temperature of the thermochemical non-equilibrium plasma for determining flow enthalpy. Because, in general, rotational freedom of the air is highly coupled with translational one, these are important properties required to evaluate flow enthalpy. In this section, the arc-heated wind tunnel and measurement approach for the rotational temperature are explained.

2.1 Facility

The ISAS 1 MW arc heater [34], which is a segmented-type arc heater, consists of an anode chamber, a cathode chamber, a constrictor section, a throat section, and a nozzle section, as shown in Fig. 1. The constrictor section is 520 mm in length and 25 mm in diameter. The throat diameter is 10 mm. The conical nozzle is 100 mm in length and its exit diameter is 25 mm.

The arc discharge is generated from a ring located in the cathode chamber and attaches on a ring in the anode chamber. Test gas is injected through the inlet tubes on the constrictor wall, and is then heated in the arc discharge. Thus, a cold gas region near the constrictor wall and a high-temperature region (i.e., the arc column) are formed in the constrictor. After choking at the throat, the arc-heated flow expands through the nozzle and is exhausted to the test (vacuum) chamber. During operation, the facility is cooled by a cooling water supply.

The test gas is supplied at mass flow rates between 10 and 30 g/s. The discharge current is between 300 and 700 A and the maximum input power of the arc heater is approximately 1 MW. Mass-averaged enthalpy of the arc-heated flow is 3–20 MJ/kg and impact pressure at the test chamber is 5–70 kPa.

The present operating parameters are listed in Table 1. So far, this condition has been applied in various ablator tests and reproductions of planetary entry environment using the wind tunnel. Heat flux is measured by a Gardon gauge sensor for every operation [35].

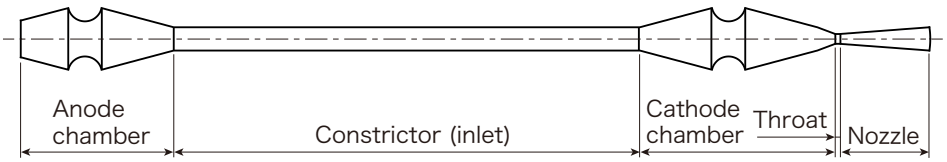

Figure 1: Configuration of the ISAS 1 MW arc heater.

Table 1: Operating parameters.

Test gas	Air
Mass flow rate, kg/s	18×10^{-3}
Total temperature of inlet gas, K	300
Input current, A	450

2.2 Emission Spectroscopy

Rotational temperature of nitric oxide (NO) of the arc-heated flow in the test chamber is measured by an emission spectroscopic measurement method. This is one of the non-intrusive measurements for plasma flows. Spectra of the γ-bands, which exist in the wavelength of 220–260 nm, are obtained. Because other strong spectra of the arc-heated flow are less apparent in this wavelength range, it is relatively easy to determine rotational temperature based on these bands.

In the present experiments, a spectroscope, MS2004i (SOL Instruments Ltd), with an intensified charge-coupled device (CCD) sensor, iSTAR DH340T-AY (ANDOR), were used. Grating of the spectroscope is 2400 lines/mm and its blaze wavelength is 225 nm. The number of pixels of the CCD sensor is 2048. Entrance slit width and exposure time of the spectroscope were set to 30 μm and 0.05 s, respectively.

The spectroscope was mounted on a traversing system. Emission spectra of the arc-heated flow were obtained at various points by focusing on measurement coordinates using a convex lens. Coordinates of the measurements whose origin were set at the nozzle exit at the centerline of the arc heater are listed in Table 2.

2.3 Temperature Determination

Spectra of γ-bands of the NO molecules strongly depend on the rotational temperature. Thus, rotational temperature can be determined through comparison between the measured spectra and the numerical spectra, which were reconstructed based on the rotational temperature.

The numerical spectra were calculated using the structured package for radiation analysis (SPRADIAN) code [36]. In the calculation, the spectral line shape was given by the Lorentzian shape with a full width at a half maximum of 0.05 nm. Spectral resolution was set to 0.1 nm. Heavy-particle-translation, vibration, electron-excitation, and electron translation-temperatures were fixed at 1000, 8000, 8000, 8000 K for all the measurement lines, respectively. Note that these temperatures are relatively insensitive to the formation of spectral shape. Only spectra produced by the NO molecules as the chemical species were considered. Radiation intensity of the spectra was normalized by the peak intensity in each wavelength range considered.

Table 2: Measurement coordinates (all dimensions are in millimeter).

(a) Line a

x	30.4	35.3	40.2	45.1	50.0	59.8	69.6
y	3.9	2.9	2.0	1.0	0.0	-2.0	-3.9
z	0.0	0.0	0.0	0.0	0.0	0.0	0.0

(b) Line b

x	75.2	80.0	84.9	90.0	94.6	99.4
y	1.2	0.0	-1.2	-2.4	-3.6	-4.9
z	0.0	0.0	0.0	0.0	0.0	0.0

(c) Line c

x	150.0	140.3	130.6
y	0.0	2.5	5.0
z	0.0	0.0	0.0

(d) Line d

x	145.0	135.3	125.6
y	0.0	2.5	5.0
z	0.0	0.0	0.0

(e) Line e

x	30.2	35.1	40.1	45.0	50.0	55.0	59.0	64.9	69.8
y	2.8	2.1	1.4	0.7	0.0	-0.7	-1.4	-2.1	-2.8
z	20.0	20.0	20.0	20.0	20.0	20.0	20.0	20.0	20.0

(f) Line f

x	67.1	71.7	76.4	81.0	85.7	90.3	95.0	99.7	104.3	109.0	113.6
y	10.9	9.08	7.3	5.5	3.6	1.8	0.0	-1.8	-3.6	-5.4	-7.3
z	20.0	20.0	20.0	20.0	20.0	20.0	20.0	20.0	20.0	20.0	20.0

(g) Line g

x	122.0	126.6	131.3	136.0	140.7	145.3	150	154.7	159.3	164.0	168.7
y	-10.7	-8.9	-7.1	-5.3	-3.6	-1.8	0.0	1.8	3.6	5.3	7.1
z	20.0	20.0	20.0	20.0	20.0	20.0	20.0	20.0	20.0	20.0	20.0

Examples of numerical and measured spectra of $\gamma(0,1)$ and $\gamma(0,2)$ bands are shown in Fig. 2. The spectra above were measured on the coordinates of $x = 150$ mm, $y = 0$ mm, and $z = 0$ mm on Line c. The double heads of the bands were confirmed from the figures. As the temperature increased, the intensity at the low wavelength side increased as well.

Rotational temperature of the NO molecules of the arc-heated flow is determined by using a curve-fitting technique between the measured spectra and the numerical spectra. In this curve-fitting process, areas formed by the intensity and wavelength of both spectra were compared. The wavelength ranges were 232.50–237.00 nm for the $\gamma(0,1)$ band and 242.00–247.75 nm for the $\gamma(0,2)$ band, respectively.

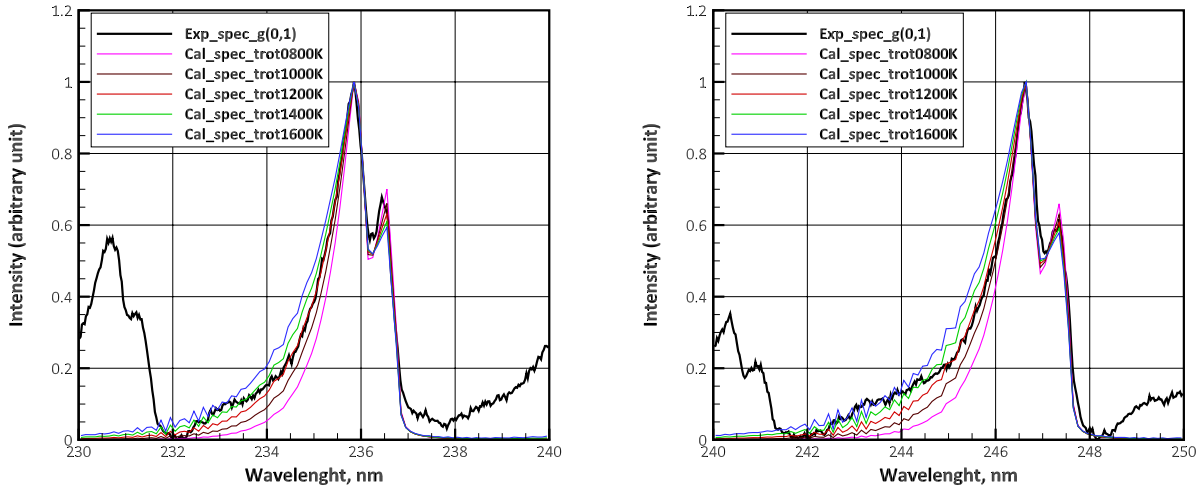

(a) γ(0,1) band.

(b) γ(0,2) band.

Figure 2: Examples of numerical and measured spectra of NO molecules in the near-Ultraviolet range

3 Modeling

In a large-scale arc-heated wind tunnel, arc column, radiation, turbulence, and expansion processes are observed. Hence, these phenomena should be reproduced appropriately. The physical and numerical models of the present numerical simulation approach were similar to those used by Takahashi (see Refs. [30, 31]). Several validations of the analysis model for the arc-heated flows are presented in the references. This section briefly describes the governing equations and models used in this study.

3.1 Governing Equations

In this study, the following assumptions were made: (1) The flow is turbulent, steady, continuum, and axisymmetric. (2) The test gas is air. (3) The flow field is in thermochemical non-equilibrium, and the temperature is separated into translational, rotational, vibrational, and electron temperatures. (4) Because the arc current is too small to induce an effective magnetic field, the Lorentz force, Hall current, and ion slip are neglected. (5) Radiation is considered.

The flow field is described using the Navier-Stokes equations extended to a thermochemical non-equilibrium flow and an equation of state. The equations consist of the total mass, momentum, total energy, species mass, rotation energy, vibration energy, and electron energy conservations. The total energy and electron-energy equations include a Joule-heating rate term that is related to the flow field and the electric field. In addition, both equations are related to the radiation calculation using the radiation term. The internal energy conservation sources are coupled with each other through the energy exchange rate terms.

The transport properties, including the viscosity, thermal conductivity, and binary diffusion coefficients for a gas mixture, were evaluated using Yos' formula [37], which is based on the first-order Chapman-Enskog approximation. The collision cross sections were obtained using Gupta's work [38] and Fertig's works [39]. The diffusion coefficients were expressed

Table 3: Chemical reactions

r	Forward		Backward
1–10	$N_2 + M$	$\rightleftharpoons$	$N + N + M$
11	$N_2 + e^-$	$\rightleftharpoons$	$N + N + e^-$
12–21	$O_2 + M$	$\rightleftharpoons$	$O + O + M$
22–31	$NO + M$	$\rightleftharpoons$	$N + O + M$
32	$NO + O$	$\rightleftharpoons$	$N + O_2$
33	$N_2 + O$	$\rightleftharpoons$	$NO + N$
34	$N + N$	$\rightleftharpoons$	$N_2^+ + e^-$
35	$O + O$	$\rightleftharpoons$	$O_2^+ + e^-$
36	$N + O$	$\rightleftharpoons$	$NO^+ + e^-$
37	$N + e^-$	$\rightleftharpoons$	$N^+ + e^- + e^-$
38	$O + e^-$	$\rightleftharpoons$	$O^+ + e^- + e^-$
39	$NO^+ + O$	$\rightleftharpoons$	$N^+ + O_2$
40	$O_2^+ + N$	$\rightleftharpoons$	$N^+ + O_2$
41	$O^+ + NO$	$\rightleftharpoons$	$N^+ + O_2$
42	$O_2^+ + N_2$	$\rightleftharpoons$	$N_2^+ + O_2$
43	$O_2^+ + O$	$\rightleftharpoons$	$O^+ + O_2$
44	$NO^+ + N$	$\rightleftharpoons$	$O^+ + N_2$
45	$NO^+ + O_2$	$\rightleftharpoons$	$O_2^+ + NO$
46	$NO^+ + O$	$\rightleftharpoons$	$O_2^+ + N$
47	$O^+ + N_2$	$\rightleftharpoons$	$N_2^+ + O$
48	$NO^+ + N$	$\rightleftharpoons$	$N_2^+ + O$
49	$N_2 + N^+$	$\rightleftharpoons$	$N_2^+ + N$

$$M = N_2,\ O_2,\ NO,\ N_2^+,\ O_2^+,\ NO^+,\ N,\ O,\ N^+,\ O^+$$

using the formula developed by Curtiss and Hirschfelder [40]. The electrical conductivity and electron component of the thermal conductivity were evaluated based on the third-order Chapman-Enskog approximations [32, 33, 41]. The collision cross sections used in the third-order approximation were obtained by Ghorui et al. [42] and by Laricchiuta et al. [43].

For chemical reactions in high-temperature air, the gas was assumed to consist of 11 chemical species, i.e., N_2, O_2, NO, N_2^+, O_2^+, NO^+, N, O, N^+, O^+, and e^-, and 49 reactions [44] as listed in Table 3 were assumed to occur. The equilibrium constants for 49 chemical reactions were calculated using the curve-fit formula and the parameters obtained by Park's model [45] and Gupta's model [38].

To express the thermal non-equilibrium, the present analysis model introduces energy transfer between the internal energy modes: translation-rotation, translation-vibration, translation-electron, rotation-vibration, rotation-electron, and vibration-electron. In addition, the energy losses and releases for the vibrations and rotations associated with the chemical reactions reveal the dissociation energies for heavy particle-impact reactions. These were obtained using a non-preferential dissociation model. The electron energy loss and release due to the electron-impact dissociation and ionization were also considered.

For the turbulence model, the shear stress transport turbulence model [46] was adopted. Using the eddy viscosity, the transport properties in the equations were replaced as follows:

(1) $\mu \rightarrow \mu + \mu_{\mathrm{t}}$, (2) $\lambda_{\mathrm{trs}} \rightarrow \lambda_{\mathrm{trs}} + \lambda_{\mathrm{t}}$, (3) $D_s \rightarrow D_s + D_{s,\mathrm{t}}$. The turbulent heat conductivity λ_{t} was evaluated using the turbulent viscosity, turbulent Prandtl number, and specific heat at a constant pressure. In addition, the turbulent diffusion coefficients $D_{s,\mathrm{t}}$ were calculated using the turbulent viscosity, turbulent Schmidt number, total density, and mass fraction. The turbulent Prandtl number and the turbulent Schmidt number were set to 0.90 and 0.90, respectively.

To calculate radiative heat flux, a radiation transport equation was modeled on the cylindrical coordinate system for integration in the spatial direction [47]. This model is a good approximation for the radiation of arc-heated flow in the constrictor where it is strongly enhanced due to high temperature gas. In addition, the three-band radiation model [25] was adopted for wavelength integration of the radiation transport equation. The computational cost of these two models is drastically lower than that of the line-by-line calculation and direct calculation in the spatial direction.

Finally, the Joule-heating rate, which expresses the heat by the arc discharge, was calculated based on Maxwell's equations and a generalized form of Ohm's law.

3.2 Computational Conditions

Figure 3 shows the computational domain of the ISAS 1 MW arc heater. A structured grid system is used for the this analysis. The number of computational grids is 385 (axial) $\times$ 75 (radial) points.

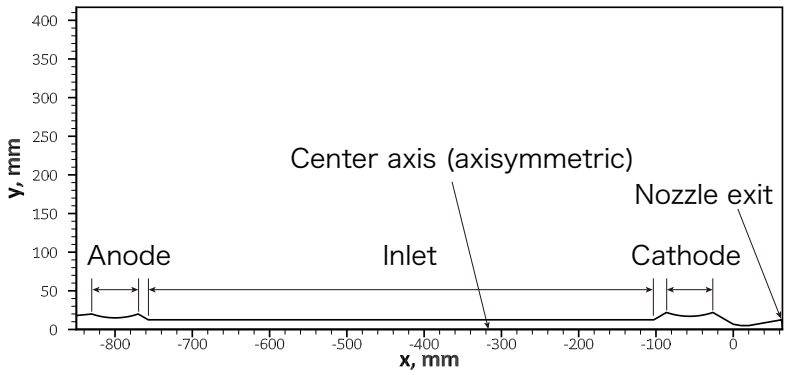

Figure 3: Computational domain for the ISAS 1 MW arc-heated flow simulation.

For the flow-field simulation, the computational boundaries consisted of the inflow boundary at the inlet, the outflow boundary at the nozzle exit, an axisymmetric boundary on the center axis, and the wall boundaries on the electrode chambers, throat section, and nozzle section. At the inflow boundary, the flow parameters were set using the mass flow rate, total temperature of the gas, and chemical components. The input parameters at the inlet are listed in Table 1. The static pressure was extrapolated from an interior point at the inflow boundary. The chemical components at the inflow were 0.765 of N_2 and 0.235 of O_2 in mass fractions. The nonslip condition for the velocity and no-pressure gradient normal to the wall were imposed at the wall boundaries. At the walls, the translational, rotational, and vibrational temperatures were fixed at 1000 K, while the electron temperature was assumed to be adiabatic. In addition, a non-catalytic wall condition, i.e., gradient free for the mass

fraction of the chemical species, was assumed. The gradient-free condition for all of the flow parameters was imposed at the outflow boundary.

Heat flux and impact pressure at the stagnation of the test model, and rotational temperature of the arc-heated flow were measured in the test chamber of 1 MW arc heater. Thus, to compare with these measurement results, it was necessary that free jet nozzle flows in the test chamber were numerically reproduced. Figure 4 is an example of the computational domain around the test model used in the present study. The number of grids was 240 (axial) $\times$ 240 (radial) points for this case. At the inflow boundary, the flow parameters, such as density, velocities, temperatures, and mass fractions of the chemical species, were given by the computational result at the nozzle exit of 1 MW arc heater. At the wall boundary, no pressure gradient normal to the wall and the nonslip conditions were imposed. Temperature of the wall was assumed to be 300 K. At the outflow boundary, the gradient-free condition of all the flow parameters was imposed. In addition, the finite catalytic condition for mass fraction at the wall was introduced. A static pressure of 100 Pa and temperature of 300 K were imposed at the ambient boundary. The mass fractions under the ambient conditions were the same as those of the air.

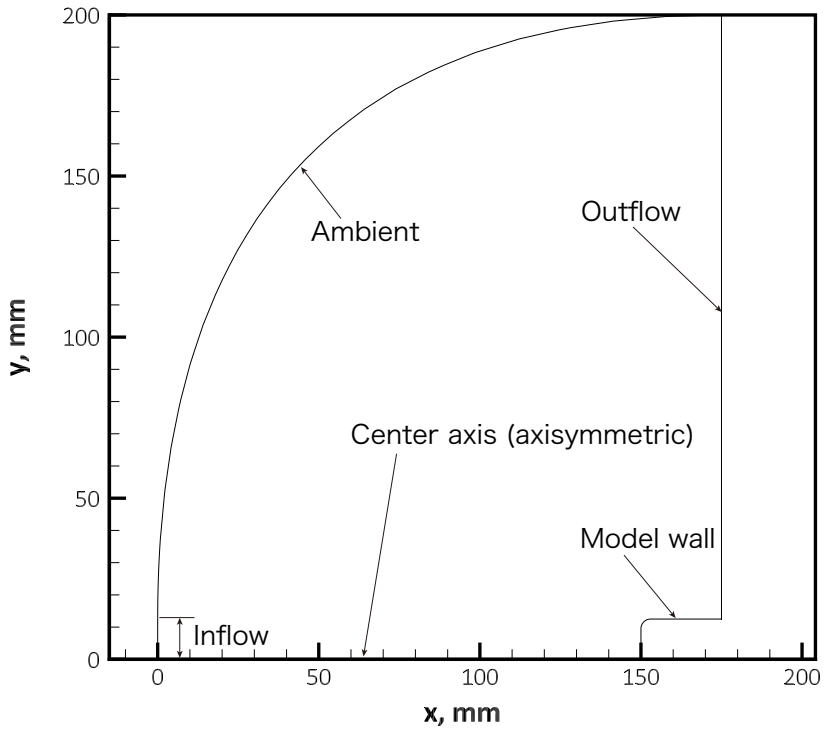

Figure 4: Computational domain and boundary conditions for nozzle flow around the test model in test chamber of 1 MW arc heater.

4 Results and Discussion

4.1 Characteristics of Arc-Heated Flow

The computational results of the arc-heated flow in the ISAS 1 MW arc heater were obtained using the present analysis model. To achieve a stable computation, a two-temperature model was used in the heating section ($x \leq 0$ m), while a four-temperature model was used in the nozzle section ($x > 0$ m). In this two-temperature model, the temperature was classified as a heavy-particle temperature (translational-rotational-vibrational temperature) and electron temperature. Because the pressure was sufficiently high and the flow field was close to the thermal equilibrium state in the heating section, the use of the two-temperature model was reasonable.

Figures 5 and 6 show the distributions of the translational temperature and Mach number in the constrictor, cathode chamber, and nozzle sections of the 1 MW arc heater, respectively. Due to the arc discharge formed in the constrictor and cathode chambers, the high-temperature region (arc column) near the center line appears. The cold gas region surrounding the arc column is formed near the walls. The flow is subsonic in the whole heating section. After choking at the throat, the Mach number monotonically increases toward the nozzle exit because of supersonic expansion in the nozzle section. The maximum Mach number reaches approximately 3.4 at the exit. Because density becomes low with the expansion in the nozzle, thermochemical non-equilibrium becomes notable. To reproduce arc discharge and supersonic expansion, it is key to appropriately model both the electric field for the arc discharge and the thermochemical non-equilibrium for the expansion process.

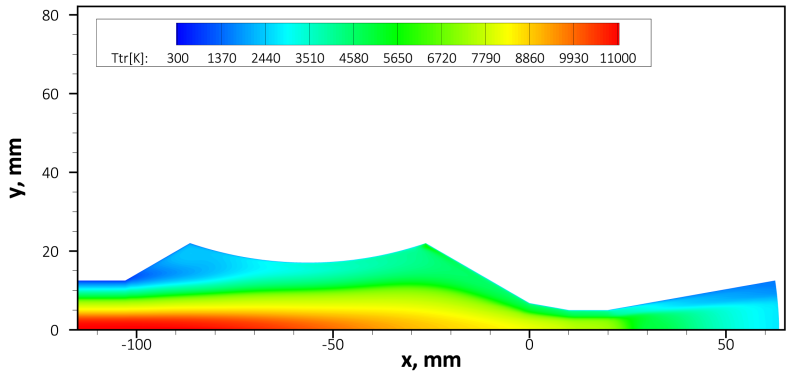

Figure 5: Distribution of translational temperature in the cathode chamber, throat, and nozzle sections.

In a large-scale arc heater, such as the 1 MW arc heater, mass, momentum, and heat transfers by turbulence and radiation are also significant. Because the plasma flows in the heating section, which is in a highly pressurized environment, its Reynolds number is high. Arc discharge causes very high-temperature air near the center line, as shown in the above figure. Figures 7 and 8 show distributions of the radiative heating rate and the ratio between turbulent and molecular viscosities, i.e., μ_t/μ, respectively. Here, the radiative heating rate was defined by $\partial q_j^{rad}/\partial x_j$. Radiation is particularly increased in the arc column in the constrictor region, where the temperature exceeds 10000 K; while radiation is low in the cathode chamber with a decrease in temperature. As well as the radiation, turbulence becomes strong

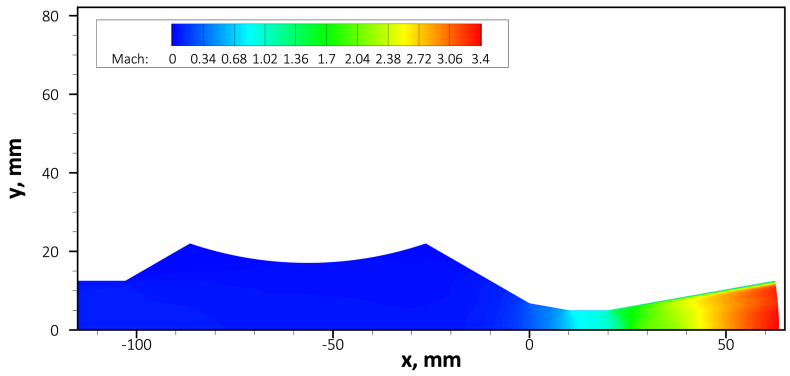

Figure 6: Distribution of Mach number in the cathode chamber, throat, and nozzle sections.

in these sections. It can be observed that the transfer mechanism of heat in the radial direction is mainly maintained by both the radiation and the turbulence. On the other hand, radiation and turbulence become low with the expansion in the nozzle section.

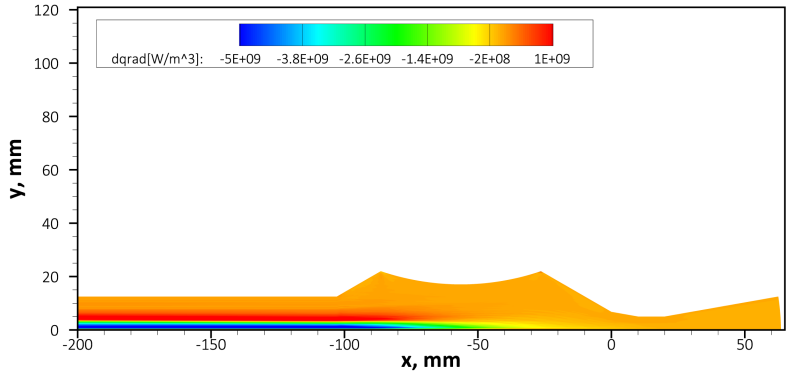

Figure 7: Distribution of radiative heating rate in constrictor, cathode chamber, throat, and nozzle sections.

To investigate the computational grids independency in the present simulations, grid studies were performed. Fine computational grids with 548 (axial) $\times$ 110 (radial) points were adopted. The relative error in the total enthalpy at the center line of the nozzle exit using the present and fine grids was within 2.7 % as listed in Table 4. This result indicates that the present computational grids sufficiently converged.

4.2 Operational Data

During experimental operation of the 1 MW arc heater, the arc voltage (V_0) between the electrodes, the pressure (p_c) in the cathode chamber, and the mass-averaged enthalpy (H_{ave}) at the nozzle exit were measured.

In the present simulation, the arc voltage was given by the electric potential drop between the anode and the cathode. The chamber pressure corresponded to the pressure value at the

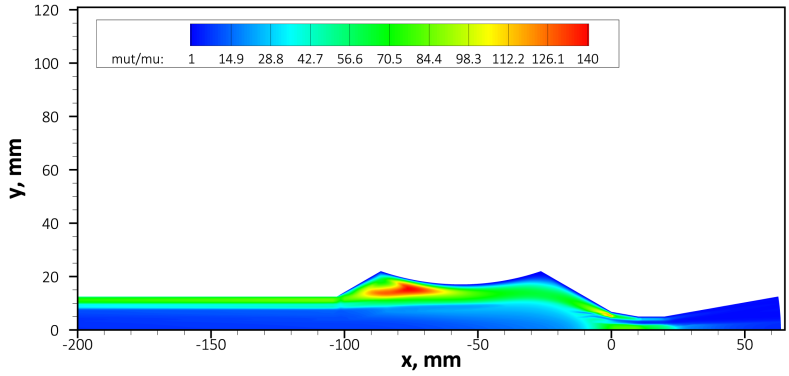

Figure 8: Distribution of ratio between turbulent and molecular viscosities in constrictor, cathode chamber, throat, and nozzle sections.

Table 4: Comparison of flow enthalpies at the nozzle exit of the arc heater in this grid study.

Case	Fine grids	Normal girds
Number of grids	548×110	385×75
Enthalpy, MJ/kg	28.47	27.71

position x=−100 mm on the center line, i.e., y=0 mm, in the cathode chamber. In addition, the mass-averaged enthalpy at the nozzle exit was determined by the following expression:

$$H_{\text{ave}} = \frac{\int \rho u h r dr}{\int \rho u r dr}. \tag{1}$$

Comparisons between these measurement data and the computational results are shown in Table 5. The computed chamber pressure and mass-averaged enthalpy show good agreements with the experimental data, although the chamber pressure is slightly overpredicted. The computed chamber pressure is strongly affected by the effective throat section area which depends on the prediction accuracy of the turbulent model. Hence, it can be observed that the turbulence model used here has sufficient prediction accuracy. On the other hand, there is a large discrepancy between the arc voltages. This is possibly because of a potential drop due to the electrical sheath near the electrode walls, which is not considered in this analysis model. Because the electrical sheath acts near the electrode walls, it does not strongly affect the whole flow field. From the comparison of the mass-averaged enthalpy, it can be judged that the electrical energy input into the flow field through the arc discharge is reproduced well. Underprediction of the arc voltage in the numerical simulation has small influence on enthalpy prediction at the nozzle exit.

Table 5: Comparison of arc voltage, chamber pressure, and mass-average enthalpy.

Case	Experiment	CFD
V_0, V	1423±6	923
p_c, MPa	0.486±0.01	0.533
H_{ave}, MJ/kg	14.3±0.4	13.4

4.3 Spectroscopic Measurements

4.3.1 Band Spectra

Emission band spectra of NO molecules in a near-ultraviolet region are measured by the present spectroscopic technique. The spectra were obtained along the lines shown in Table 2 using the traverse device mentioned earlier. Assuming that the flow field is axisymmetric two-dimensional, measurement lines projected in the two-dimensional plane are given by Lines a—g, shown in Fig. 9, in which the origin coordinate is set to the nozzle exit on the center line of the 1 MW arc heater. Thus, the region where y=−12.5–12.5 mm at x=0 mm in this figure corresponds to the nozzle exit. This figure also includes the distribution of the rotational temperature obtained by the present numerical analysis in the test chamber.

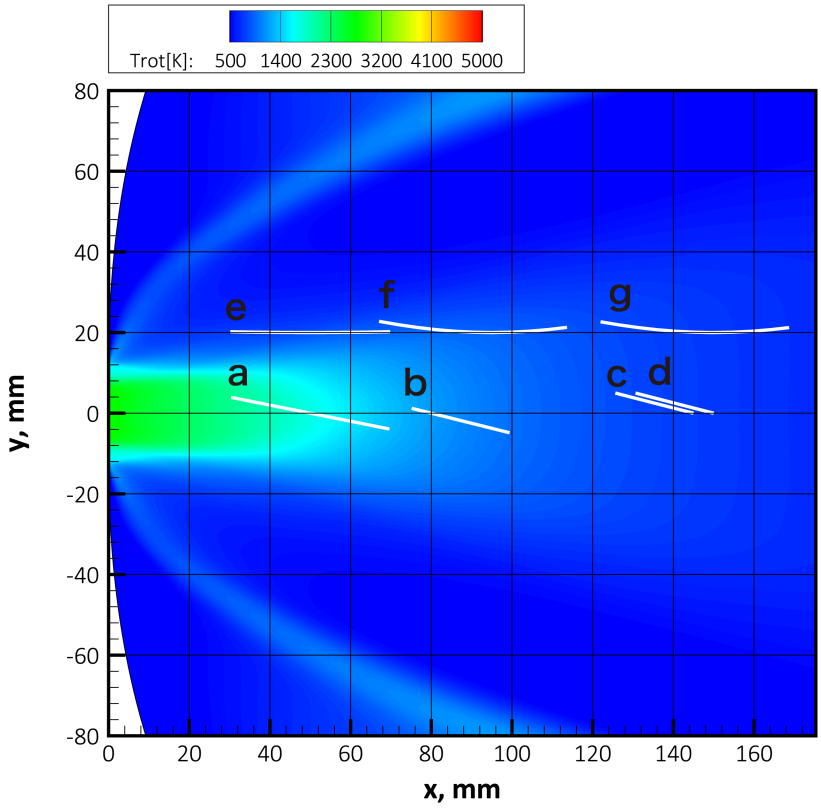

Figure 9: Measurement lines scanned by the traverse device in the test chamber overlapping computed rotational temperature distribution.

Figure 10 shows the NO band spectra in a wavelength range between 220 nm and 260 nm

at the x=50 mm and y=0 mm in Line a. Spectra of γ-bands and δ-bands are observed. Reproducibility of spectra measurements is good, although the figure is not presented. Because the $\gamma(0,1)$ and $\gamma(0,2)$ spectra are remarkable compared with other spectra, these spectra were adopted to determine the NO molecules rotational temperature by a curve-fitting technique.

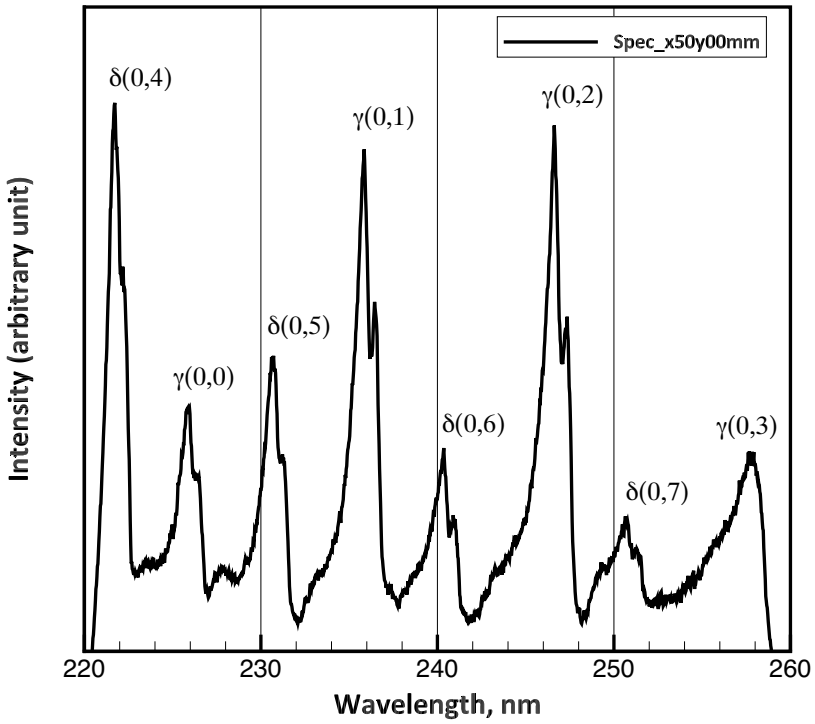

Figure 10: Band spectra in wavelength range between 220 and 260 nm at x=50 mm and y=0 mm.

4.3.2 Rotational Temperature

Rotational temperature profiles along the seven lines measured by the spectroscopic technique against $\gamma(0,1)$ and (0,2) bands are shown in Figs. 11(a) and 11(b). These figures also include the computed results of translational, rotational, vibrational, and electron temperatures obtained by the present analysis in the test chamber of 1 MW arc heater. The spectra at each measurement coordinate were obtained in three different runs of the wind tunnel experiment. The error bars of the measured rotational temperatures in the figures indicate their standard deviations.

The measured rotational temperatures monotonically decrease as the distance from the nozzle exit becomes larger. This is attributed to a decrease in translational temperature with strong expansion in the test chamber where ambient pressure becomes approximately 100 Pa in operation. In general, the rotational energy mode of high-temperature air is strongly coupled with the translational mode. Thus, as translational temperature decreases, rotational temperature tends to decrease.

The computed results show strong thermal non-equilibrium between the translational–rotational temperatures and the electron–vibrational temperatures. Because relaxation between translational energy and electron energy modes is relatively low, the electron and vibrational temperatures do not decrease significantly even if supersonic expansion occurs.

The computed rotational temperatures at all the lines, except for Line e, show good agreement with the measured ones. This indicates that the present analysis model well reproduces the thermal enthalpy component at the core of the arc-heated flow. However, the surrounding flow of the core near the nozzle exit, as shown in the comparison between the measured and predicted results at Line e, is insufficiently reproduced. It may be possible to improve the diffusion models and chemical models in the expansion region for a more accurate prediction. The present analysis model adopts relatively simple models for describing chemical reactions in terms of computational cost. As indicated by Colonna et al. [48–50], models that consider a metastable state for a more detailed discussion of this issue should be introduced in the future.

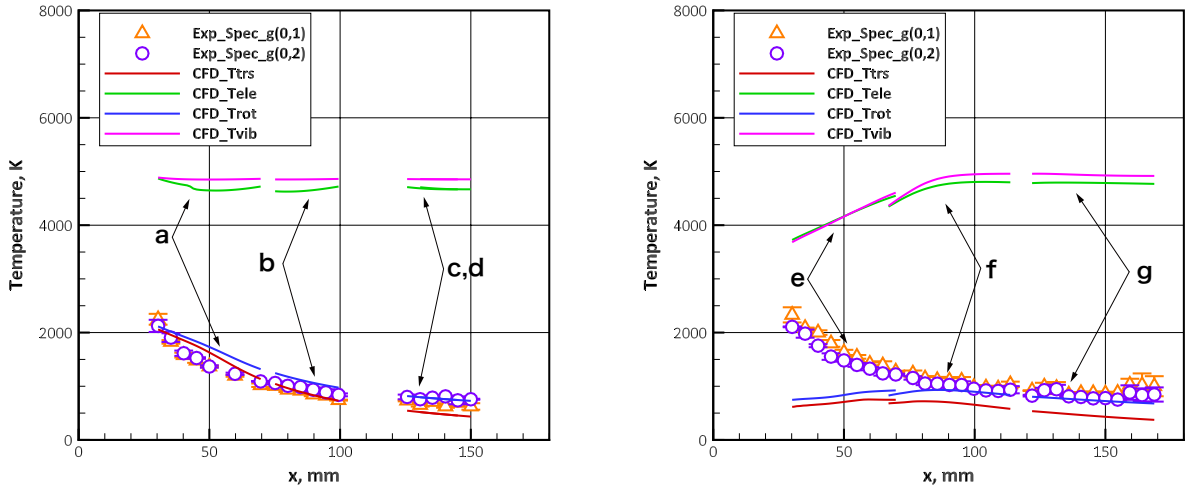

(a) Lines a, b, c, and d.

(b) Lines e, f, and g.

Figure 11: Comparison of rotational temperature profiles between the experiments and the present numerical analysis in the test chamber of the 1 MW arc heater.

4.4 Probe Measurements

As reported in Ref. [35], heat flux and stagnation impact pressure profiles along the center line in the test chamber of the 1 MW arc heater were measured by a Gardon gauge and a pressure sensor, respectively. In the experiment, the heat flux and the impact pressure were obtained by 25 mm flat-faced cylinder models. The measurement positions were several points from x=25 mm to 200 mm downstream of the nozzle exit. In order to compare the present numerical analysis results with the measured data, flow field simulations around the flat-faced cylinder models exposed to the arc-heated flow were carried out as mentioned earlier.

The convective heat flux at the wall can be obtained using the following expression:

$$q_{\mathrm{w}}^{\mathrm{con}} = \lambda_{\mathrm{trs}}\frac{\partial T_{\mathrm{trs}}}{\partial n} + \lambda_{\mathrm{rot}}\frac{\partial T_{\mathrm{rot}}}{\partial n} + \lambda_{\mathrm{vib}}\frac{\partial T_{\mathrm{vib}}}{\partial n} + \lambda_{\mathrm{ele}}\frac{\partial T_{\mathrm{ele}}}{\partial n} + \rho\sum_{s}^{ns} h_s D_s \frac{\partial X_s}{\partial n}. \tag{2}$$

The first four terms in the right hand side of the above equation are the thermal components, whereas the last one is the chemical component that is affected by the surface catalysis. In general, the surface catalysis has a strong impact on the heat flux of the arc-heated flows. In this study, the surface catalysis, i.e., the finite catalytic condition, is evaluated by the following expression:

$$\rho D_s \frac{\partial C_s}{\partial n} = \gamma\sqrt{\frac{kN_{\mathrm{A}}T_{\mathrm{w}}}{2\pi M_s}}\rho_s, \tag{3}$$

where ρ, D_s, C_s, M_s, and n are the density, the effective diffusion coefficient of species s, mass fraction, molar mass, and coordinate in the normal direction to the wall surface, respectively. In addition, k and N_{A} are the Boltzmann constant and the Avogadro constant, respectively. Recombination reactions of atomic nitrogen and atomic oxygen, i.e., N+N→N_2 and O+O→O_2, were considered. The recombination coefficient γ of both reactions, which is generally a value between 0 and 1, was set to 0, 0.001, 0.005, 0.01, 0.1, and 1.0. Here, the conditions of γ=0 and γ=1 correspond to the non-catalytic wall and the fully-catalytic wall, respectively.

Comparisons of heat flux and impact pressure profiles between the experiments and the present analysis results are shown in Figs. 12(a) and 12(b), respectively. Peak heat flux and impact pressure in the experiment were approximately 15 MW/m^2 and 75 kPa, respectively. Thus, the 1 MW arc heater can simulate aerodynamic heating environments of the Hayabusa sample return capsule at a reentry speed of 11.8 km/s and a high-velocity reentry capsule with rigid flare at 14.5 km/s [51]. The measured heat flux and pressure rapidly decrease as the test model becomes far from the nozzle exit. This is caused by the expansion in the test chamber.

From the computational results, it was found that the heat flux is very sensitive to the recombination coefficient γ, while the impact pressure is insensitive. The computed profiles of impact pressure reproduce the tendency of the measured pressure well. However, slight discrepancies appear, which are caused by overprediction of pressure at the cathode chamber, as shown in Table 5. When γ is within 0.005–0.01, the computed heat flux also shows good agreement with the measured data. This is deduced to be in a reasonable order of magnitude. Marschall [52] reported that the recombination coefficient of constantan (i.e., the alloy of Cu and Ni) adopted in the Gardon gauge was 0.046±0.017 for the reaction between O_2 and O. According to Nawaz [53], copper oxides, such as CuO and Cu_2O, were in the order of 10^{-2}. Discrepancy of heat flux between γ=1 and γ=0.1 becomes low. This is mainly because the recombination reactions almost finish at γ=0.1. The present results indicate that this arc heater has a potential to achieve a peak heat flux of approximately 20 MW/m^2, if the surface recombination reactions produced by the catalysis fully occur.

4.5 Flow Enthalpy in Arc Heater

The flow enthalpy in this study was defined by the following expression:

$$h = e_{\mathrm{trs}} + e_{\mathrm{rot}} + e_{\mathrm{vib}} + e_{\mathrm{ele}} + \sum_{s=1}^{ns} C_s \Delta h_s^0 + \frac{1}{2}u_i u_i + \frac{p}{\rho}, \tag{4}$$

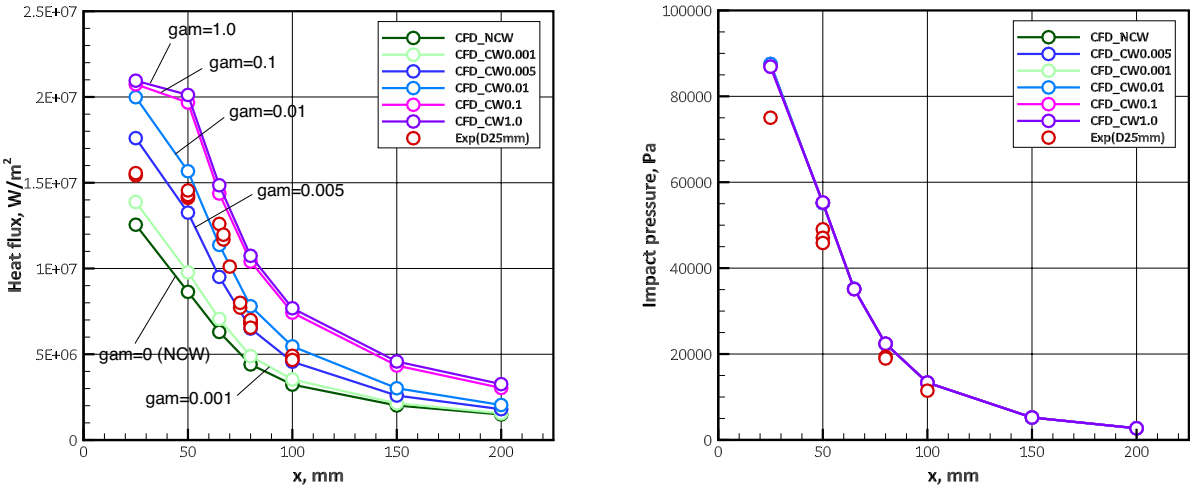

(a) Heat flux.

(b) Stagnation impact pressure.

Figure 12: Comparison of heat flux and stagnation impact pressure profiles between the experiments and the present numerical analysis along the center line in the test chamber of the 1 MW arc heater.

where the terms from the first to the fourth in the right-hand side are thermal components. The fifth, the sixth, and the seventh terms are chemical, kinetic, and pressure components of the flow enthalpy, respectively.

Figures 13(a), 13(b), and 13(c) show the computed radial profiles of the flow enthalpy at the constrictor section (x=−100 mm), the throat section (x=15 mm), and the nozzle exit of the 1 MW arc heater, respectively (see also Fig. 3). Each component of the enthalpy, in addition to the total enthalpy, is illustrated in the figures. The dominant component of the flow enthalpy is the chemical component in these three sections. Furthermore, the following components are the thermal component at the constrictor and throat, and the kinetic component at the nozzle, respectively. It was found that the electrical energy by the arc discharge almost inputs into the chemical energy at the constrictor. In the cathode chamber, flow enthalpy is smoothed in the radial direction and dissipated on the wall by the radiation and turbulence. Total enthalpy distributions at the throat and nozzle exit are similar, although ratio of each component is different. Due to the expansion process throughout the nozzle, thermal and pressure components are low. Moreover, the chemical component near the center axis decreases by recombination reactions. The total enthalpy reached a peak value of approximately 28 MJ/kg at the center line at the nozzle and rapidly decreases toward the nozzle wall. Because mixing in the radial direction in the nozzle is insignificant, this non-uniformity is mainly attributed to the arc-heated flow in the cathode chamber, which is caused by arc discharge.

It can be observed that the computed enthalpy near the center line accurately reproduces the experiments for the present operating condition. The rotational temperature is strongly equilibrated with the translational one, which is related to the thermal components of the flow enthalpy. Note that the vibrational and electron energies are relatively lower than the translational energy. The heat flux obtained by the Gardon gauge is well correlated with the chemical component in addition to the thermal component. The impact pressure is strongly related to the kinetic and pressure components. Thus, as presented in the previous sections,

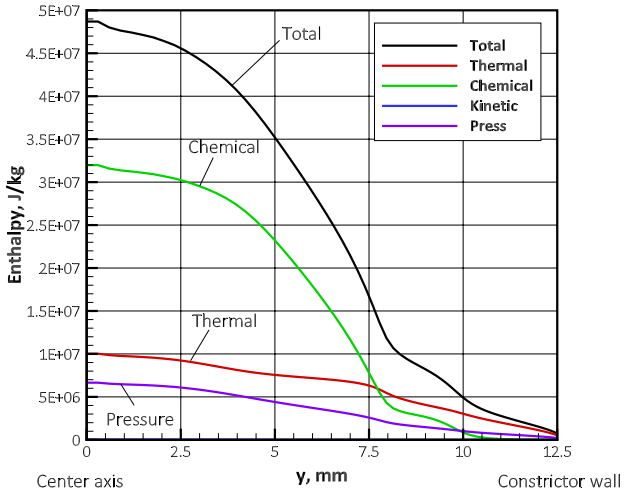

(a) Constrictor.

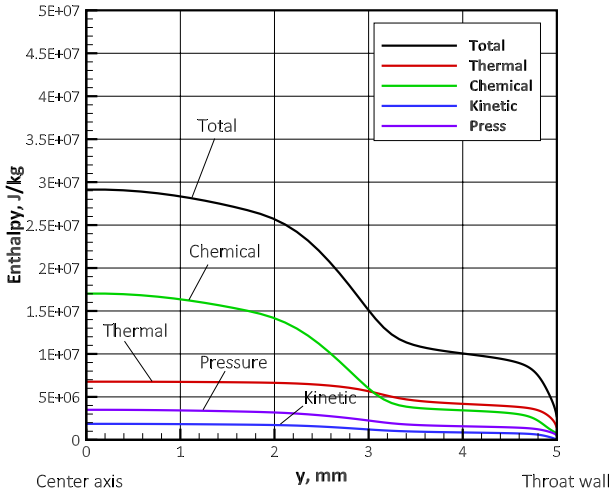

(b) Throat.

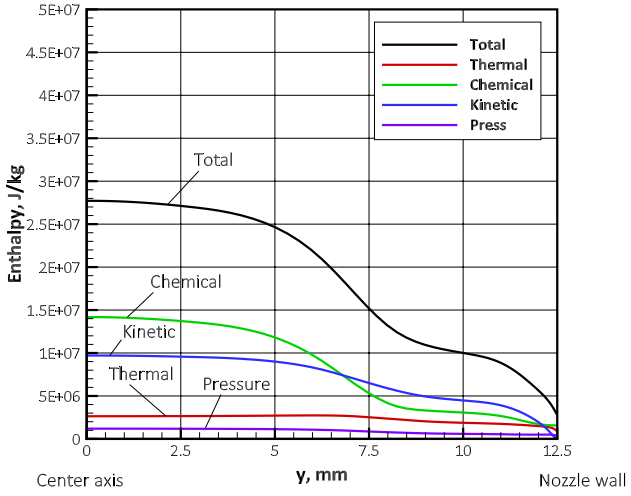

(c) Nozzle exit.

Figure 13: Radial profiles of flow enthalpy in 1 MW arc heater.

this analysis model shows good agreements with the measured values, and it is concluded that prediction performance is sufficient. On the other hand, there is slight uncertainty, arising from the surface catalysis of the Gardon gauge, in determining a chemical component of flow enthalpy. There are almost no measurement data to validate the numerical analysis model for predicting the heat flux and impact pressure of the surrounding flow. These issues will be left for one of the future studies.

Radial profiles of temperatures, velocity, and mole fractions at the nozzle exit are shown in Figs. 14(a) and 14(b), respectively. The heating section, the high-temperature and high-velocity core region, and the cold gas region surrounding the core are confirmed. This is particularly remarkable for chemical compositions, as shown in the figure. Dominant chemical species are the atomic species such as N and O in the core flow, while the molecular species of N_2 are present in the surrounding flow. Note that the decrease in electrons in the core flow is caused by recombination reactions between ionic species and electrons. It was found that

diffusion in the radial direction proceeds insufficiently in the nozzle. The highly non-uniform distribution of the flow enthalpy shown in Fig. 13 is mainly attributed to that of the chemical compositions.

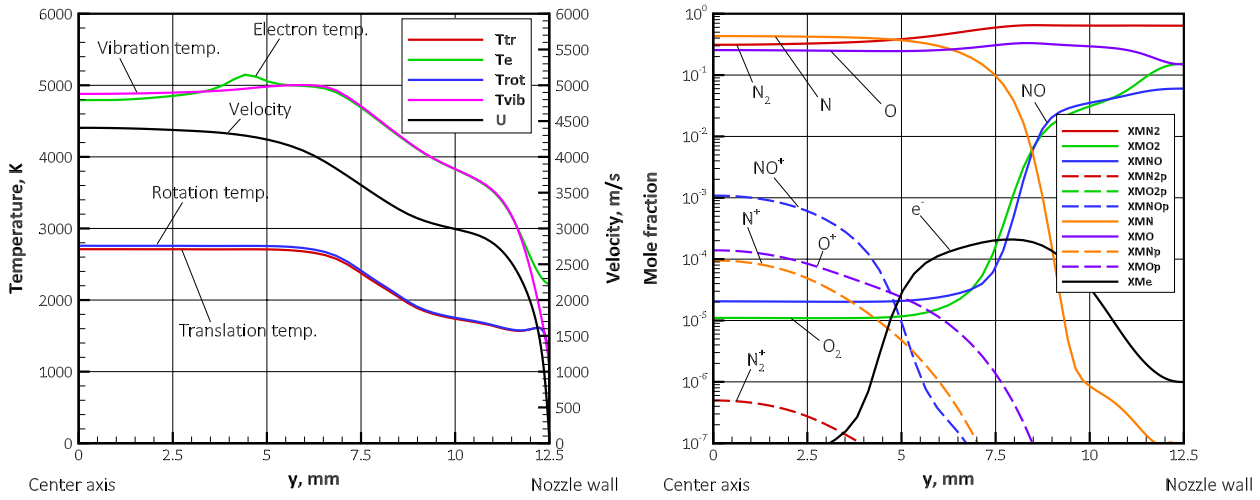

(a) Temperatures and velocity.

(b) Mole fractions.

Figure 14: Radial profiles of temperatures and mole fractions at the nozzle exit.

Assuming that the probe surface is fully catalytic, the flow enthalpy can be evaluated using HRM based on the heat flux and impact pressure measured using the probe technique, which is given by

$$q_{\mathrm{w}}\sqrt{\frac{R_{\mathrm{eff}}}{p}} = K\left(h - h_{\mathrm{w}}\right), \tag{5}$$

where K=6.62×10^{-4} W/(m$^{3/2}$·Pa$^{1/2}$·J/kg) for air. The enthalpy at the wall, h_{w}, is negligible compared with the flow enthalpy (h). As the flat-face probe was used in the experiment, the correlated nose radius (R_{eff}) of the hemispherical shape was adopted according to Zoby's study [54]. This was given by R_{eff}=R/0.285, where the body radius (R) is 12.5 × 10^{-3} m. The flow enthalpy obtained using HRM was 21 MJ/kg at x=50 mm and y=0 mm. As the flow enthalpy of 28 MJ/kg, obtained using CFD, at the nozzle exit did not decrease downstream, the flow enthalpy obtained using HRM was underestimated. However, in the experiments, the probe surface material comprising constantan was not fully catalytic. Based on the comparison with the CFD results (Fig. 12(a)), the heat flux obtained using the probe technique possibly underestimated the fully catalytic case, thereby causing the discrepancy between the HRM and CFD results.

5 Conclusions

The flow enthalpy of an arc-heated wind tunnel is an important parameter for aerospace applications. In particular, for the development of reentry capsules such as the Hayabusa sample return capsule, the determination of flow properties including the enthalpy at the arc jet generated by the arc-heated wind tunnel are highly demanded. In this study, the flow

enthalpy of a 1 MW arc-heated wind tunnel, which is a large-scale segmented-type facility, was determined using a computational science approach. The rotational temperature of nitric oxide molecules, in addition to the heat flux and impact pressure, was obtained using the spectroscopic technique. By comparing the experimental data, it was discovered that the present numerical analysis model appropriately reproduced the core flow of the arc-heated flows. Based on the computed and measured results, the values of total enthalpy and each component, i.e., thermal, chemical, kinetic, and pressure were presented. The dominant components of enthalpy of the free jet nozzle flow in the test chamber were chemical and kinetic components. Moreover, from these results, we deduced that the flow enthalpy at the nozzle exit was approximately 28 MJ/kg. This study also suggested the possibility of a method for determining the flow enthalpy of arc-heated flows using the computational science approach.

However, because measurement data were lacking, enthalpy of the surrounding flow of the arc-heated flow in the test chamber was insufficiently obtained. Further validation of the analysis model for arc-heated flow is also necessary to describe appropriately the transfer mechanism of heat and momentum in the radial direction. Further improvements in determining the flow enthalpy distribution are left for future study.

Acknowledgments

The authors would like to thank Prof. Takeharu Sakai (Tottori University, Japan) for the helpful discussions regarding the present numerical analysis modeling and enthalpy determination. The authors also would like to thank Mr. Manabu Matsunaga (Hokkaido University) for his valuable cooperation. This work was supported by JSPS KAKENHI Grant Numbers 17K14871 and 17KK0123. The wind tunnel experiments were conducted at an arc wind tunnel facility at the Institute of Space and Astronautical Science, Japan Aerospace Exploration Agency, which is an inter-university research institute. The computations were performed using the computational facilities at the Research Institute for Information Technology, Kyushu University.

Appendix: Spectra Reconstructed using CFD results

Figures 15(a) and 15(b) compare the $\gamma(0,1)$ band spectra of NO molecules based on the measurements and computational analysis. The computed intensities were reconstructed based on the temperature and number density of NO obtained from the CFD results. These intensities were normalized using the peak value in the wavelength range of 230–240 nm. At x=50 mm and y=0 mm in the test chamber, the intensity obtained using CFD was higher than that of the measurement at the low-wavelength side, while the intensity of the second head of the band at a wavelength of 236.5 nm was lower, which were attributed to the overprediction of the rotational temperature and the underprediction of the electron temperature, respectively. Meanwhile, the CFD intensity at x=150 mm and y=0 mm well reproduced the experiment.

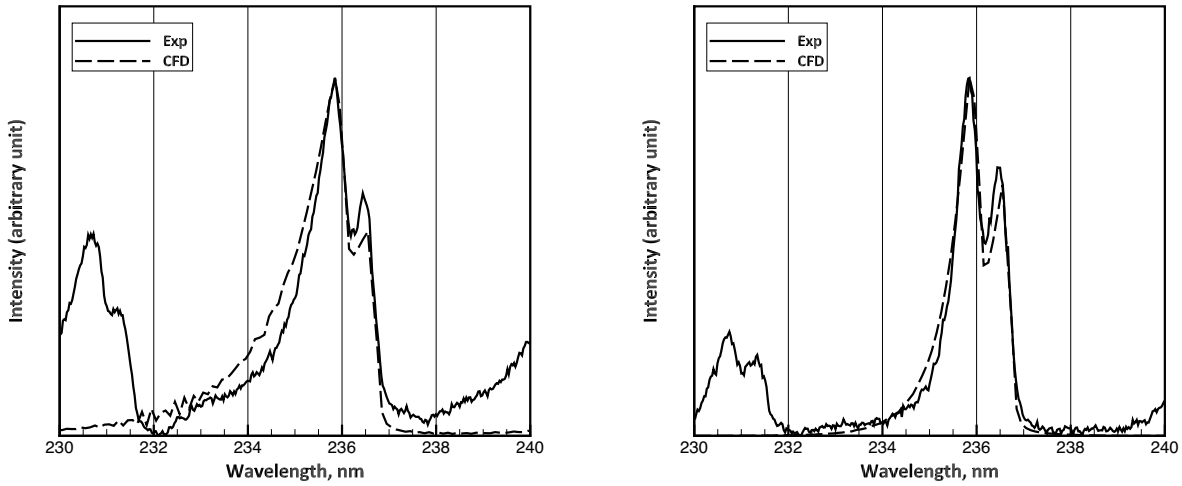

(a) x=50 mm and y=0 mm.

(b) x=150 mm and y=0 mm.

Figure 15: Comparison of $\gamma(0,1)$ band spectra of NO molecules based on the measurements and CFD results.

References

[1] Campagnola, S., Yam, C. H., Tsuda, Y., Ogawa, N., and Kawakatsu, Y., "Mission analysis for the Martian Moons Explorer (MMX) mission," *Acta Astronautica*, Vol. 146, 2018, pp. 409–417.

[2] Funase, R., Mori, O., Shirasawa, Y., and Yano, H., "Trajectory Design and System Feasibility Analysis for Jovian Trojan Asteroid Exploration Mission Using Solar Power Sail," *Transactions of the Japan Society for Aeronautical and Space Sciences, Aerospance Technology Japan*, Vol. 12, No. ists29, 2014, pp. Pd_85–Pd_90.

[3] Tsou, P., Brownlee, D. E., McKay, C. P., Anbar, A. D., Yano, H., Altwegg, K., Beegle, L. W., Dissly, R., Strange, N. J., and Kanik, I., "LIFE: Life investigation for Enceladus a sample return mission concept in search for evidence of life," *Astrobiology*, Vol. 12, No. 8, 2012, pp. 730–742.

[4] Otsu, H., Suzuki, K., Fujita, K., and Abe, T., "Assessment of Forebody and Backbody Radiative Heating Rate of Hypervelocity Reentry Capsule," ISAS Report SP 17, Institute of Space and Aeronautics Science, Sagamihara, Japan, March 2003.

[5] Fujita, K., Suzuki, T., Matsuyama, S., Yamada, T., and Abe, S., "Numerical Reconstruction of HAYABUSA Sample Return Capsule Flight Environment," *AIAA Paper 2011-3477*, 2011.

[6] Olynick, D., Chen, Y.-K., and Tauber, M. E., "Aerothermodynamics of the Stardust Sample Return Capsule," *Journal of Spacecraft and Rockets*, Vol. 36, No. 3, May-June 1999, pp. 442–462.

[7] Gupta, R. N., "Aerothermodynamic Analysis of Stardust Sample Return Capsule with Coupled Radiation and Ablation," *Journal of Spacecraft and Rockets*, Vol. 37, No. 4, July-August 2000, pp. 507–514.

[8] Abe, K., Kameyama, T., Kihara, H., Nishida, M., Ito, K., and Tanno, H., "Computation and Experiment of Nonequilibrium Nozzle Flow of Arc-heated Air," *Journal of Thermophysics and Heat Transfer*, Vol. 19, No. 4, 2005, pp. 428–434.

[9] Fletcher, D. G., "Arcjet flow properties determined from laser-induced fluorescence of atomic nitrogen," *Applied optics*, Vol. 38, No. 9, 1999, pp. 1850–1858.

[10] Grinstead, J. H., Diver, D. M., and Raiche, G. A., "Radial Profiles of Arcjet Flow Properties Measured with Laser-Induced Fluorescence of Atomic Nitrogen," *AIAA Paper 2003-400*, 2003.

[11] Takayanagi, H., Matsui, M., Komurasaki, K., Ochimizu, H., and Arakawa, Y., "Arc wind-tunnel flow diagnostics by cavity-enhanced absorption spectroscopy," *AIAA journal*, Vol. 47, No. 5, 2009, pp. 1195–1199.

[12] Takahashi, Y., Abe, T., Takayanagi, H., Mizuno, M., Kihara, H., and Abe, K., "Advanced Validation of Nonequilibrium Plasma Flow Simulation for Arc-Heated Wind Tunnels," *Journal of Thermophysics and Heat Transfer*, Vol. 28, No. 1, January-March 2014, pp. 9–17.

[13] Winter, M. W., Prabhu, D. K., Raiche, G. A., Terrazas-Salinas, I., and Hui, F. C. L., "Emission Spectroscopic Measurement with an Optical Probe in the NASA Ames IHF Arc Jet Facility," *AIAA Paper 2012-1016*, 2012.

[14] Zander, F., Löhle, S., Hermann, T., and Fulge, H., "Fabry–Perot spectroscopy for kinetic temperature and velocity measurements of a high enthalpy air plasma flow," *Journal of Physics D: Applied Physics*, Vol. 50, No. 33, 2017, pp. 335202.

[15] Gülhan, A., Esser, B., Koch, U., Fischer, M., Magens, E., and Hannemann, V., "Characterization of High-Enthalpy-Flow Environment for Ablation Material Tests Using Advanced Diagnostics," *AIAA Journal*, Vol. 56, No. 3, 2018, pp. 1072–1084.

[16] Steffens, L., Koch, U., Esser, B., and Gülhan, A., "Characterization of weakly ionized argon flows for radio blackout mitigation experiments," *Progress in Flight Physics–Volume 9*, Vol. 9, EDP Sciences, 2017, pp. 335–348.

[17] Marvin, J. G. and Pope, R. B., "Laminar Convective Heating and Ablation in the Mars Atmosphere," *AIAA Journal*, Vol. 5, No. 2, February 1967, pp. 240–248.

[18] E637-05, A., "Standard Test Method for Calculation of Stagnation Enthalpy from Heat Transfer Theory and Experimental Measurements of Stagnation-Point Heat Transfer and Pressure," *ASTM International, West Conshohocken, PA*, 2016.

[19] Park, C., Raiche, G. A., Driver, D. M., Olejniczak, J., Terrazas-Salinas, I., Hightower, T. M., and Sakai, T., "Comparison of enthalpy determination methods for an arc-jet facility," *Journal of thermophysics and heat transfer*, Vol. 20, No. 4, 2006, pp. 672–679.

[20] Löhle, S., Auweter-Kurtz, M., and Eberhart, M., "Local enthalpy measurements in a supersonic arcjet facility," *Journal of thermophysics and heat transfer*, Vol. 21, No. 4, 2007, pp. 790–795.

[21] Hermann, T., Löhle, S., Zander, F., and Fasoulas, S., "Measurement of the aerothermodynamic state in a high enthalpy plasma wind-tunnel flow," *Journal of Quantitative Spectroscopy and Radiative Transfer*, Vol. 201, 2017, pp. 216–225.

[22] Colonna, G. and Capitelli, M., "Boltzmann and Master Equations for Magnetohydrodynamics in Weakly Ionized Gases," *Journal of Thermophysics and Heat Transfer*, Vol. 22, No. 3, July-Sept. 2008, pp. 414–423.

[23] Sakai, T., Sawada, K., and Mitsuda, M., "Application of Planck-Rosseland-Gray Model for High-Enthalpy Arc Heaters," *Journal of Thermophysics and Heat Transfer*, Vol. 15, No. 2, April-June 2001, pp. 176–183.

[24] Lee, J.-P., Kim, C., and Kim, K.-H., "Accurate Computations of Arc-Heater Flows Using Two-Equation Turbulence Models," *Journal of Thermophysics and Heat Transfer*, Vol. 21, No. 1, Jan.-Mar. 2007, pp. 67–76.

[25] Sakai, T., "Computational Simulation of High-Enthalpy Arc Heater Flows," *Journal of Thermophysics and Heat Transfer*, Vol. 21, No. 1, Jan.-Mar. 2007, pp. 77–85.

[26] Prabhu, D., Saunders, D., Oishi, T., Skokova, K., Santos, J., Fu, J., Terrazas-Salinas, I., Carballo, J., and Driver, D., "CFD Analysis Framework for Arc-Heated Flowfields I: Stagnation Testing in Arc-Jets at NASA ARC," *41st AIAA Thermophysics Conference*, 2009, p. 4080.

[27] Prabhu, D., Saunders, D., Tang, C., Terrazas-Salinas, I., Carballo, J., and Driver, D., "CFD Analysis Framework for Arc-Heated Flowfields II: Shear Testing in Arc-Jets at NASA ARC," *41st AIAA Thermophysics Conference*, 2009, p. 4081.

[28] Hightower, T. M., Balboni, J. A., Donald, C. L. M., Anderson, K. F., and Martinez, E. R., "Enthalpy by Energy Balance for Aerodynamic Heating Facility at NASA Ames Research Center Arc Jet Complex," *Proceedings of the 48th International Instrumentation Symposium*, ISA TP02-AERO-2000, Instrumentation, Systems, and Automation Society, San Diego, CA, USA, 2002.

[29] Takahashi, Y., Kihara, H., and Abe, K., "Numerical Investigation of Nonequilibrium Plasma Flows in Constrictor- and Segmented-Type Arc Heaters," *Journal of Thermophysics and Heat Transfer*, Vol. 24, No. 1, 2010, pp. 31–39.

[30] Takahashi, Y., Kihara, H., and Abe, K., "The Effects of Radiative Heat Transfer in Arc-Heated Nonequilibrium Flow Simulation," *Journal of Physics D: Applied Physics*, Vol. 43, No. 18, 2010, pp. 185201.

[31] Takahashi, Y., Kihara, H., and Abe, K., "Turbulence and Radiation Behaviours in Large-Scale Arc Heaters," *Journal of Physics D: Applied Physics*, Vol. 44, No. 8, 2011, pp. 085203.

[32] Katsurayama, H. and Abe, T., "Thermochemical Nonequilibrium Modeling of a Low-Power Argon Arcjet Wind Tunnel," *Journal of Applied Physics*, Vol. 113, 2013, pp. 053304.

[33] Yu, M., Yamada, K., Takahashi, Y., kai Liu, and Zhao, T., "Flow-Field Differences and Electromagnetic-Field Properties of Air and N2 Inductively Coupled Plasmas," *Physics of Plasmas*, Vol. 23, No. 12, 2016, pp. 123523.

[34] Yamada, T. and Inatani, Y., "Arc Heating Facility and Test Technique for Planetary Entry Missions," *The Institute of Space and Astronautical Science report. SP Aerodynamics, Thermophysics, Thermal Protection, Flight System Analysis and Design of Asteroid Sample Return Capsule*, Vol. 17, 2003, pp. 147.

[35] Shimoda, T. and Yamada, K., "Arc Heating Wind Tunnel Facility in ISAS/Japan and the activity to update and improve it for Further Sample Return Missions," 46th International Conference on Environmental Systems, 2016.

[36] Fujita, K. and Abe, T., "SPRADIAN, Structured Package for Radiation Analysis: Theory and Application," ISAS Report 669, Institute of Space and Aeronautics Science, Sagamihara, Japan, Sep. 1997.

[37] Yos, J. M., "Transport Properties of Nitrogen, Hydrogen Oxygen and Air to 30,000 K," *TRAD-TM-63-7,* Research and Advanced Development Division, AVCO Corp., 1963.

[38] Gupta, R. N., Yos, J. M., Thompson, R. A., and Lee, K.-P., "A Review of Reaction Rates and Thermodynamic and Transport Properties for an 11-Species Air Model for Chemical and Thermal Nonequilibrium Calculations to 30000 K," *NASA RP-1232*, Aug. 1990.

[39] Fertig, M., Dohr, A., and Frühauf, H.-H., "Transport Coefficients for High-Temperature Nonequilibrium Air Flows," *Journal of Thermophysics and Heat Transfer*, Vol. 15, No. 2, April-June 2001, pp. 148–156.

[40] Curtiss, C. F. and Hirschfelder, J. O., "Transport Properties of Multicomponent Gas Mixture," *Journal of Chemical Physics*, Vol. 17, No. 6, June 1949, pp. 550–555.

[41] Devoto, R. S., "Simplified Expressions for the Transport Properties of Ionized Monatomic Gases," *Physics of Fluid*, Vol. 10, No. 10, 1967, pp. 2105–2112.

[42] Ghorui, S. and Das, A. K., "Collision integrals for charged-charged interaction in two- temperature non-equilibrium plasma," *Physics of Plasmas*, Vol. 20, No. 9, 2013, pp. 093504.

[43] Laricchiuta, A., Bruno, D., Capitelli, M., Catalfamo, C., Celiberto, R., Colonna, G., Diomede, P., Giordano, D., Gorse, C., Longo, S., Pagano, D., and Pirani, F., "High temperature Mars atmosphere. Part I: transport cross sections," *The European Physical Journal D*, Vol. 54, 2009, pp. 607–612.

[44] Park, C., "Assessment of a Two-Temperature Kinetic Model for Dissociating and Weakly Ionizing Nitrogen," *Journal of Thermophysics and Heat Transfer*, Vol. 2, No. 1, Jan.-March 1988, pp. 8–16.

[45] Park, C., *Nonequilibrium Hypersonic Aerothermodynamics*, Wiley, New York, 1990.

[46] Menter, F. R., Kuntz, M., and Langtry, R., "Ten Years of Industrial Experience with the SST Turbulence Mode," *Turbulence, Heat and Mass Transfer 4, ed: K. Hanjalic, Y. Nagano, and M. Tummers, Begell House, Inc.*, 2003, pp. 625–632.

[47] Kesten, A. S., "Radiant Heat Flux Distribution in a Cylindrically-Symmetric Nonisothermal Gas with Temperature-Dependent Absorption Coefficient," *J. Quant. Spectrosc. Radiat. Transfer*, Vol. 8, 1968, pp. 419–434.

[48] Colonna, G., Pietanza, L., and D'Ammando, G., "Self-consistent collisional-radiative model for hydrogen atoms: Atomatom interaction and radiation transport," *Chemical Physics*, Vol. 398, No. Supplement C, 2012, pp. 37 – 45, Chemical Physics of Low-Temperature Plasmas (in honour of Prof Mario Capitelli).

[49] Colonna, G., D'Ammando, G., Pietanza, L., and Capitelli, M., "Excited-state kinetics and radiation transport in low-temperature plasmas," *Plasma Physics and Controlled Fusion*, Vol. 57, No. 1, 2014, pp. 014009.

[50] Colonna, G., D'Ammando, G., and Pietanza, L., "The role of molecular vibration in nanosecond repetitively pulsed discharges and in DBDs in hydrogen plasmas," *Plasma Sources Science and Technology*, Vol. 25, No. 5, 2016, pp. 054001.

[51] Takahashi, Y. and Yamada, K., "Aerodynamic-Heating Analysis of Sample-Return Capsule in Future Trojan-Asteroid Exploration," *Journal of Thermophysics and Heat Transfer*, Vol. 32, No. 3, July 2018, pp. 547–559.

[52] Marschall, J., Copeland, R., Hwang, H., and Wright, M., "Surface catalysis experiments on metal surfaces in oxygen and carbon monoxide mixtures," *44th AIAA Aerospace Sciences Meeting and Exhibit*, 2006, p. 181.

[53] Nawaz, A., Driver, D. M., Terrazas-Salinas, I., and Sepka, S., "Surface catalysis and oxidation on stagnation point heat flux measurements in high enthalpy arc jets," *44th AIAA Thermophysics Conference*, 2013, p. 3138.

[54] Zoby, E. V. and Sullivan, E. M., "Effects of corner radius on stagnation-point velocity gradients on blunt axisymmetric bodies," *Journal of Spacecraft and Rockets*, Vol. 3, No. 10, 1966, pp. 1567–1567.